

Mn single atoms for one-electron photoozonation of aqueous organics

Jing Wang ^{a,b}, Zhaomeng Xu ^{a,b}, Yanjun Xu ^c, Shenning Liu ^d, Jiakai Qiu ^a, Zhuan Wang ^c, Yuxian Wang ^d, Yuxiang Weng ^c, Hongbin Cao ^a, Shaobin Wang ^{e,*}, Yongbing Xie ^{a,b,***}

^a Chemistry & Chemical Engineering Data Center, Institute of Process Engineering, Chinese Academy of Sciences, Beijing 100190, China

^b School of Chemical Engineering, University of Chinese Academy of Sciences, Beijing 100049, China

^c Beijing National Laboratory for Condensed Matter Physics, CAS Laboratory of Soft Matter Physics, Institute of Physics, Chinese Academy of Sciences, Beijing 100190, China

^d State Key Laboratory of Heavy Oil Processing, State Key Laboratory of Petroleum Pollution Control, China University of Petroleum-Beijing, Beijing 102249, China

^e School of Chemical Engineering, The University of Adelaide, Adelaide, SA 5005, Australia



ARTICLE INFO

Keywords:

Single-atom catalysts
Localized charge carriers
One-electron reduction
Hydroxyl radical
Photocatalytic ozonation

ABSTRACT

Photocatalytic ozonation offers a potential approach for highly efficient organic degradation by *in-situ* generation of reactive $\cdot\text{OH}$ via electron reduction of ozone. Herein, we synthesized a Mn single atom photocatalyst for promoting the $\cdot\text{OH}$ generation from O_3 activation under visible light irradiation. Theoretical calculation and experimental studies reveal that Mn single atoms on carbon nitride significantly promote the excitation and transfer of photo-generated electrons, making charge carriers enriched around MnN_4 sites and shortening their migration path to participate in surface reactions. Meanwhile, Mn single atoms serve as adsorption and catalytic sites for O_3 , favoring a fast one-electron-reduction reaction kinetics. More importantly, the trade-off between the number of available electrons and active sites in photocatalytic performance was observed from regulating the density of Mn single atoms. This work offers an intriguing regulation strategy for enriching surface charges on single atom catalyst interface toward efficient $\cdot\text{OH}$ production and removal of aqueous organics.

1. Introduction

Artificial photosynthesis of hydroxyl radicals ($\cdot\text{OH}$, $E_0=2.80 \text{ V}_{\text{NHE}}$) has been deemed a promising technology for aqueous organics degradation with renewable energy in wastewater remediation [1–3]. In principle, $\cdot\text{OH}$ mainly originates from the reaction between charge carriers (CB- e^- and VB- h^+) and acceptors (O_2 and H_2O) [4,5]. O_2 has been widely used to capture photo-generated electrons to produce $\cdot\text{OH}$ through a three-electron-reduction path ($\text{O}_2 \rightarrow \text{O}_2^- \rightarrow \text{HO}_2^- \rightarrow \text{H}_2\text{O}_2 \rightarrow \cdot\text{OH}$), which is a tandem reaction with low efficiency [6]. By contrast, O_3 exhibits a higher solubility and stronger thermodynamical ability in the capture of electrons than O_2 , which may greatly intensify $\cdot\text{OH}$ generation [7,8]. Meanwhile, the robust one-electron-reduction route ($\text{O}_3 \rightarrow \text{O}_3^- \rightarrow \text{HO}_3^- \rightarrow \cdot\text{OH}$) can maximize the conversion efficiency from both available photoelectrons and O_3 molecules to $\cdot\text{OH}$ [9]. In this regard, photocatalytic ozonation driven by sunlight is highly attractive for organics degradation in real applications. However, O_2 and O_3 simultaneously exist in the gas phase, and the competitive three-electron reduction of O_2 would lead to an inefficient utilization of electrons [10].

To this end, unique manipulation of both electronic structures of catalytic active centers and properties of a semiconductor material is necessary to ensure the abundant supply of electrons and a high selectivity of one-electron reduction pathway.

As a potential candidate photocatalyst, polymeric carbon nitride (PCN, bandgap of 2.7 eV) has been proven effectively in the reduction of O_3 under visible light irradiation, but its activity is still far from the requirement for the practical application [11–13]. Generally, the low dielectric permittivity in PCN strengthens the Coulomb interaction in an electron-hole pair and shortens the exciton diffusion length [14]. As a result, effective excitation mostly occurs on the PCN surface or nearby, due to the short diffusion distance of charge carriers [15]. The yield of $\cdot\text{OH}$ from O_3 reduction is closely related to the number of available photogenerated electrons. Thus, the precise regulation of the PCN surface properties is very important to enrich the surface concentration of photoinduced charge carriers by suppressing their rapid recombination and enhance the apparent performance of the catalyst. Additionally, a sluggish surface reaction kinetics also limits the photocatalytic activity because it is unable to consume the surviving charge carriers with a

* Corresponding author.

** Corresponding author at: Chemistry & Chemical Engineering Data Center, Institute of Process Engineering, Chinese Academy of Sciences, Beijing 100190, China.

E-mail addresses: shaobin.wang@adelaide.edu.au (S. Wang), ybxe@ipe.ac.cn (Y. Xie).

short lifetime. Thus, construction of surface O_3 active sites with tailored geometrical and electronic properties is necessary [16].

Recently, single-atom catalysts (SACs) have received widespread attention due to their unique electronic structures and maximized atom utilization [17–19]. Compared with a nanosized metal with the same loading, SACs can provide more reaction sites to inhibit undesirable electron-hole recombination by decreasing travel distance, and better confine the catalytic reaction to the desired route [20–24]. More importantly, immobilization of atomically dispersed metals on PCN may effectively increase the local charge concentration, promote charge migration and facilitate surface reactions [15,25–27]. Teng et al. found that single Sb atoms could simultaneously act as the electron acceptors and O_2 activation sites, which facilitated the formation of μ -peroxide to notably promote a two-electron oxygen reduction reaction [24]. Su et al. observed that a high activity of heterogeneous photocatalytic activation of H_2O_2 was achieved by concentrating photogenerated electrons on iron single-atom sites [26]. Inspired by these findings, we believe that the enrichment of surface photogenerated electrons around O_3 activation sites is promising to improve electron utilization on specially designed PCN-based SACs through accelerating interfacial charge transfer and favoring surface reaction kinetics.

Herein, we developed a series of PCN-supported Mn SACs (Mn-CN) to generate $\bullet OH$ under visible light irradiation for organics degradation. Notably, the photocatalytic performance is improved greatly, and the catalyst with higher density of Mn single atoms exhibits a better performance, but inferior mass activity due to the trade-off between the number of available electrons and active sites. Experimental investigations and theoretical calculations suggest that the incorporation of Mn promotes the excitation and transfer of photo-promoted electrons and create a high concentration of local electrons around MnN_4 sites. Meanwhile, Mn single atoms act as the adsorption and catalytic activation sites of O_3 , greatly favoring the one-electron reduction path for O_3 activation. Thus, the adequate supply of available electrons around catalytic sites ensures efficient $\bullet OH$ production. This concept of enhancing surface charge concentration with SACs provides a strategy to develop more efficient environmental catalysts for wastewater remediation.

2. Experimental

2.1. Materials and Chemicals

$MnCl_2 \bullet 4 H_2O$, dicyanamide, methanol, oxalic acid (OA), benzoic acid (BA), bisphenol A (BPA), p-nitrophenol (PNP), and p-benzoquinone (PBQ) were obtained from Sinopharm Chemical Reagent Co., Ltd., China. Ultrapure gases of argon and oxygen (> 99.999%) were supplied by Beijing Qianxi Gas Co., Ltd., China. Those chemicals were of an analytical grade at least with no further purification. In this work, all the test solutions were prepared using ultrapure water (18.2 $M\Omega \bullet cm$).

2.2. Preparation of catalysts

The Mn-CN catalysts were prepared based on our previously reported method [28]. Dicyandiamide (1 g) and a certain amount of $MnCl_2 \bullet 4 H_2O$ (0.5, 0.75, 1.0 and 1.25 mmol) were added into deionized water (20 mL) and stirred sufficiently. Then the solution is heated to 120 °C to remove water completely. The dried mixture was then ground and heated to 600 °C at a rate of 10 °C/min and maintained at the temperature for 3 h under argon atmosphere. For comparison, PCN was prepared under the same synthesis conditions without adding $MnCl_2 \bullet 4 H_2O$.

2.3. Characterization methods

The crystal phases were investigated by X-ray diffraction (XRD) (X' PERT-PRO MPD, Philips, Holland) using a Cu $K\alpha$ source. The surface

structures of catalysts were characterized by the Fourier transform infrared (FTIR) spectroscopy with a T27-Hyperion-Vector 22 spectrometer (Bruker, Germany). The catalyst morphology and composition were characterized by using the high-angle annular dark-field scanning transmission electron microscopy (HAADF-STEM) with a Titan Cubed Themis 60–300 STEM-mapping and transmission electron microscopy (TEM, JEM-2100 f, JEOL, Japan). X-ray photoelectron spectroscopy (XPS) was carried out using an Al $K\alpha$ source and the binding energy was calibrated with C 1 s peak at 284.8 eV (Thermo Fisher Scientific, USA). The real Mn concentrations in the catalysts were determined by an inductively coupled plasma-atomic emission spectrometer (ICP-OES, iCAP 6300, Thermo, USA). N_2 adsorption–desorption isotherms and pore size distributions were conducted to obtain a specific surface area (Autosorb-iQ, Quantachrome, USA).

The synchrotron X-ray absorption spectroscopy (XAS) was carried out at the Beijing Synchrotron Radiation Facility (BSRF) using the 4B9A station, and IFEFFIT software was utilized to analyze all the XAS data. A spectrofluorometer was used to measure the photoluminescence (PL) emission and time-resolved PL spectra excited at 330 nm by a Horiba Jobin Yvon NanoLOG-TCSPC, USA. The absorbance was measured using an ultraviolet–visible spectrophotometer (Cary 5000 instrument, Varian, USA). Reactive radicals in the reaction were analyzed by electron paramagnetic resonance using 5, 5-dimethyl-1-pyrroline (DMPO) as the spin-trapping agent (EPR, ELEXSYS E500, Bruker, Germany)

Measurements of ultrafast transient absorption spectroscopy (TAS) were performed by using a pump-probe system equipped with a Ti: sapphire femtosecond laser (35 fs, 800 nm, 1 kHz) as the laser source. The excitation laser (400 nm, 1 mJ/cm²) was used to excite PCN and Mn-CN, where the excitation beam was generated by frequency doubling the Ti: sapphire laser (800 nm) through a BBO crystal. The photogenerated charge carriers were probed in the visible to near-IR regions, covering the range of 400 nm to 1.4 μ m. Visible probe light was produced by focusing the 800 nm laser onto a CaF_2 crystal plate, while near-IR probe light was generated by focusing onto a sapphire crystal plate. Two fiber optic spectrometers were used to detect the visible probe light ranging from 400 to 800 nm (AvaSpec-ULS2048CL-EVO, Avantes) and the near-IR light from 0.9 to 1.4 μ m (AvaSpec-NIR256-1.7-HSC-EVO, Avantes).

A computer-controlled electrochemical station was used for electrochemical tests in a three-electrode system (CHI760E, Chenhua Instrument Co., Ltd., China). A saturated calomel electrode and platinum wire were used as the reference and counter electrodes, respectively. For a rotating ring-disk electrode (RDE) test, an IPS-RRDE/RDE was used to measure the oxygen reduction reaction (ORR) performance. The samples for the ORR test were prepared as follows: a mixture of 10 mg catalysts, 0.08 mL Nafion (5 wt%, Alfar Aesar) and 4 mL isopropanol was stirred for 60 min under ultrasonic oscillation. Then the suspension (12 μ L) was dropped onto an electrode of a glassy carbon (GC) disk, for a catalyst density of 98 μ g cm^{-2} . After drying for 15 min at 80 °C, the working electrodes for the RDE test were obtained. Linear sweep voltammetry (LSV) was firstly conducted at different voltages of $-1 \sim 0$ V in N_2 saturated solution at a sweep rate of 5 $mV s^{-1}$, and then in O_3 saturated solution.

For all (photo)electrochemical characterizations, a Xe lamp (350 W) was used as the light source. H_2SO_4 was used to adjust the pH of electrolyte (O_2 -saturated Na_2SO_4 solution, with a volume of 200 mL and the concentration of 0.05 M). In a light on-off cycle, the transient photocurrent was measured. Electrochemical impedance spectroscopy (EIS) was performed at open circuit voltage of 10 mV over a frequency range of $10^6 \sim 10^{-2}$ Hz in dark and illumination.

2.4. Catalytic reactions tests

Photocatalytic ozonation for the elimination of OA and other organics were carried out in a cylindrical borosilicate glass reactor (450 mL) at 25 °C. A gas flow of O_2/O_3 was bubbled continuously into

the reactor through a porous plate at an O_3 concentration of 30 mg/L and a flow rate of 100 mL/min. An ozone generator (COM-AD-01, Anseros) was used to produce O_3 and its concentration was measured by an Ozomat GM6000PRO ozone analyzer (Anseros). Visible light (420–750 nm) at a flux of 360 mW/cm², generated by a CEL-NP2000 Xenon lamp (300 W, Aulight Co., Ltd., China), was used to irradiate the solution. The reaction solution is 300 mL consisted of 0.1 g/L of catalyst and 2 mM of OA. Before reaction, an adsorption-desorption equilibrium was established by magnetically stirring the mixture for 30 min in dark. For organic analysis, a high-performance liquid chromatography (HPLC) equipment of Agilent series 1200 (USA) was employed, which was equipped with a UV-Vis detector and a Zorbax SB-Aq column. A mobile phase composed of aqueous 10 mM H_3PO_4 and methanol (80/20, v/v) was used. In addition, a Jena TOC-VCPh analyzer was employed for analysis of total organic carbon (TOC) and the Indigo blue method was used for analysis of dissolved O_3 in solution [29].

2.5. Computation details for calculations

The total energies were obtained by density functional theory (DFT) using projected augmented wave (PAW) potentials within the generalized gradient approximation (GGA) in a the PBE formulation from a Vienna Ab Initio Package (VASP) [30–32]. A plane wave basis set was used with a cutoff of kinetic energy at 400 eV [33,34]. The electronic energy was considered to be self-consistent at the energy change smaller than 10^{-5} eV. The Gaussian smearing method was used in partial occupancies of the Kohn–Sham orbitals with a width of 0.05 eV. Atomic positions were relaxed until the residue force on each atom was smaller than 0.02 eV/Å. The description of the dispersion interactions was studied with Grimme's DFT-D³ methodology [35]. In Brillouin zone sampling by the Γ point, the equilibrium lattice constants of rectangular 1D PCN unit cell separated by a vacuum layer in the depth of 15 Å were optimized to be $a=16.900$ Å and $b=12.680$ Å, which was used for further calculations. To relax this surface model, we used the gamma point in the Brillouin zone for k-point sampling and allowed all atoms for relaxing.

The O_3 adsorption energy was calculated by the following equation.

$$E_{\text{ads}} = E_{\text{O}_3/\text{surf}} - E_{\text{surf}} - E_{\text{O}_3(\text{g})}$$

Where, E_{ads} , $E_{\text{O}_3/\text{surf}}$, E_{surf} , and $E_{\text{O}_3(\text{g})}$ are the energies of adsorption, surface adsorbate O_3 , the clean surface, and an isolated O_3 molecule, respectively, in a cubic periodic box with a $1 \times 1 \times 1$ Monkhorst-Pack k-point grid and a side length of 20 Å for Brillouin zone sampling.

3. Results and Discussion

3.1. Catalyst synthesis and characterizations

Single-atom Mn catalysts were prepared by a one-step calcination method, and Mn metal loading was manipulated by changing the amount of $MnCl_2 \bullet 4 H_2O$ precursor. ICP-OES tests show that the real Mn contents of the as-prepared SACs were at 4.0, 7.3, 8.9, and 10.1 wt% (namely xMn-CN, x=4.0, 7.3, 8.9, and 10.1, respectively). The chemical component of PCN and support of Mn-CNs is $C_3N_{4.5}H_{1.5}$ (Table S1), suggesting the imbedding of Mn single atoms did not cause vacancies. The XRD patterns of the catalyst samples showed only one broad peak at 27.3°, which was assigned to the (002) plane reflection generated by the layered periodic structure of tri-s-triazine (Figure S1) [36]. The absence of a peak at 13.0° may be attributed to the loading of Mn single atoms, which destroyed the in-plane repetition period. Some additional weak peaks arise in the XRD patterns of Mn-CNs with an increased Mn concentration, which can be assigned to melem-analogous compounds rather than Mn species [37,38]. This is probably because an excessive Mn content suppresses the polymerization process from melem to

carbon nitride.

The FTIR spectra (Figure S2) of Mn-CNs show no obvious difference in the range of 810, 1245–1573 and 3190 cm⁻¹, suggesting that the typical peaks of carbon nitride skeleton hardly changed after incorporation of Mn atoms [39]. Notably, a new vibration band at around 2150 cm⁻¹ attributed to cyano terminal groups (C≡N) arises in the spectra of all Mn-CN samples, which may be resulted from the reaction of Mn^{2+} with the amine groups in the tri-s-triazine rings during the high temperature thermal treatment process. [40] The XPS characterization shows the peaks of C, N and Mn elements (Figure S3) in Mn-CNs. In addition, a stronger C2 peak (286.1 eV) and a right-shifted N1 peak (398.8 eV) corresponding to the C≡N bond and the sp^2 C≡N-C bond are observed in Mn-CNs, which may be attributed to the formation of Mn-N bond (Figures S4–S5) [23]. N_2 adsorption–desorption isotherms show that the incorporation of Mn atoms slight reduced the surface area of PCN, but it gradually increased with the increase of Mn content. This is probably associated with changes in tri-s-triazine units with the participation of Mn^{2+} as indicated by XRD and FTIR results (Figure S6).

Fig. 1a–b show the representative images of aberration-corrected high-angle annular dark-field scanning transmission electron microscopy (AC-HAADF-STEM). Mn species exists as single-atoms (bright dots) both on 4.0Mn-CN and 10.1Mn-CN. Energy-dispersive X-ray spectroscopy further confirms the uniform composition and dispersion of Mn, N, and C atoms in all the samples (Fig. 1c and Figure S7). All the above results indicate that the Mn metal atoms were successfully isolated and implanted into PCN.

Since all the Mn-CN samples exhibit the single-atom dispersion, we subsequently probe the local structures and oxidation states of Mn species by using X-ray absorption fine structure (XAFS) spectroscopy. The X-ray absorption near-edge structure (XANES) spectra at the Mn K-edge of Mn foil, Mn_2O_3 , $MnCl_2$ and Mn-CNs are shown in Fig. 1d. The absorption edge of 4.0Mn-CN overlapped with that of $MnCl_2$, confirming that the average valence state of Mn species in the Mn-CN is +2, which is further indicated by the XPS results due to the appearance of a specific shakeup satellite peak at 646 eV (Figure S8). [28] A slightly right shift of the absorption edge occurs with an increased Mn content, and the change of the Mn oxidation state of Mn-CNs is negligible. In the Fourier-transform extended X-ray absorption fine structure (FT-EXAFS) spectra (Fig. 1e), all the samples of Mn-CNs present a major peak at 1.70 Å, which can be ascribed to the coordination of Mn atoms with nitrogen [28]. Both the peak location and intensity exhibit a negligible change with the increasing content of Mn, reflecting a similar coordination environment. The comparison with Mn foil and oxide references shows that there is no apparent Mn–Mn bond in all the Mn-CN samples, which identifies the atomic dispersion of Mn species.

The wavelet-transform EXAFS (WT-EXAFS) analysis was conducted to visually distinguish the neighboring coordination of Mn atoms. Obviously, the WT contour plots of the Mn-CN materials displayed only one intensity maximum at ~ 5 Å⁻¹ in k-space, corresponding to the Mn–N scattering path (Fig. 1f and S9). The typical WT signals related to Mn–Mn contribution at ~ 9 Å⁻¹ was not detected in all samples, confirming the isolated features of Mn species. Least-squares EXAFS curve fitting analyses were conducted to investigate the local coordination structure of Mn-CNs (Fig. 1g–j), and the extracted fitting parameters are presented in Table S2. As shown, Mn coordination number in the Mn–N bond was estimated to be around 4 with a bond length of 2.17 Å.

3.2. Catalytic evaluation

The photocatalytic ozonation performance of the Mn-CN materials was evaluated by OA elimination, because OA has a low reaction rate with O_3 ($k_{O_3} = 0.04$ M⁻¹·s⁻¹) but it is readily decomposed by $^{\bullet}OH$ [41]. As depicted in Fig. 2a, adsorption tests demonstrated that a negligible amount of OA was adsorbed on both PCN and 4.0Mn-CN. In terms of OA oxidation, only 20.7% removal of OA within 60 min was achieved in the Vis/ O_3 system with PCN. In contrast, as high as 100% OA degradation

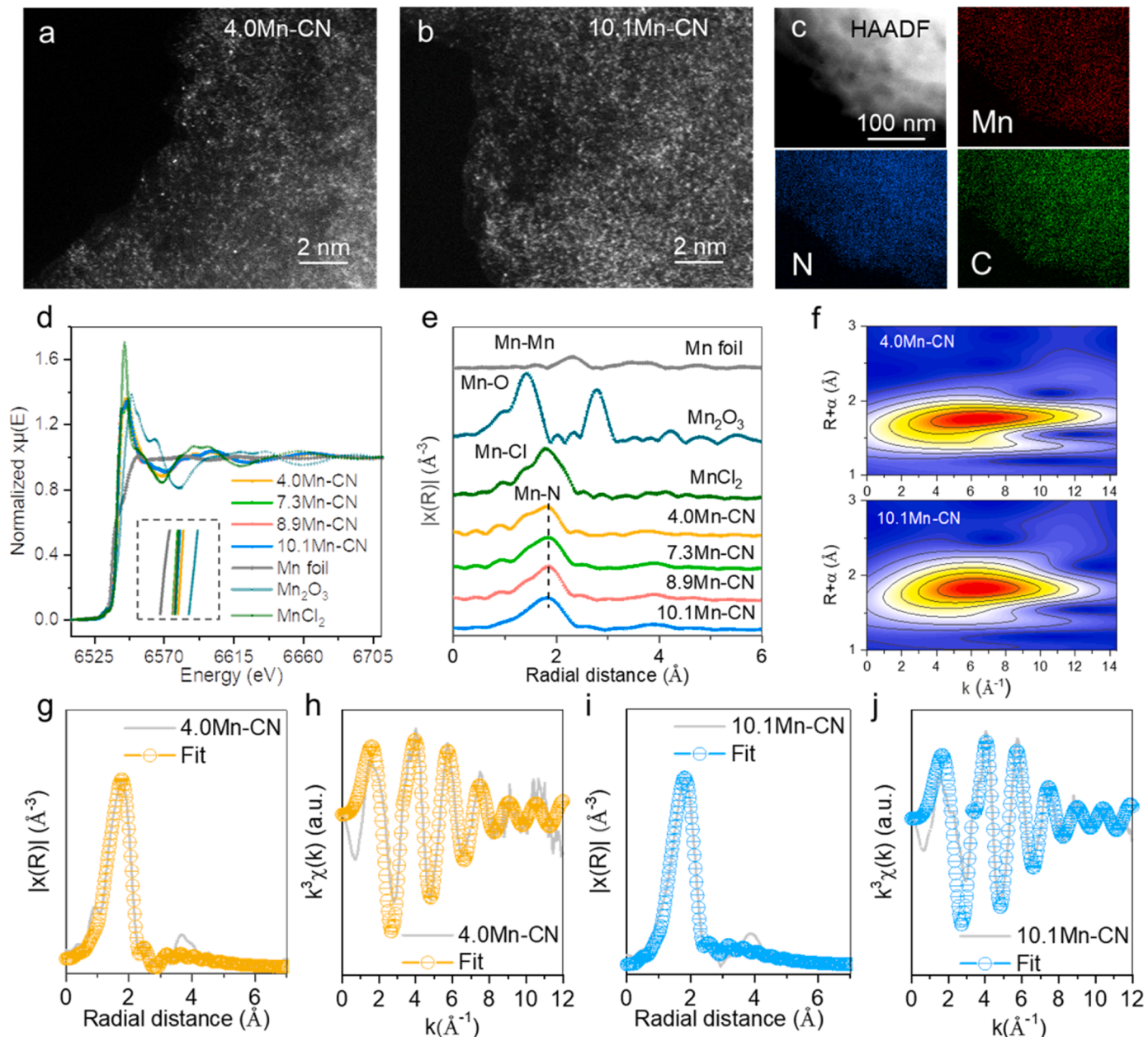


Fig. 1. Atomic-resolution HAADF-STEM images of 4.0Mn-CN (a), and 10.1Mn-CN (b). Elemental mappings of 4.0Mn-CN (c) (Mn-red, N-blue and C-green). Mn K-edge XANES spectra of Mn foil, Mn_2O_3 , MnCl_2 and Mn-CNs (d). Fourier transform K-edge spectra of Mn-CNs and their reference samples (e). Wavelet transforms of the k^3 -weighted EXAFS signals of 4.0Mn-CN and 10.1Mn-CN (f). Corresponding FT-EXAFS fitting curves of 4.0Mn-CN (g) and 10.1Mn-CN (j) at R space. Corresponding FT-EXAFS fitting curves of 4.0Mn-CN (h) and 10.1Mn-CN (i) at K-space.

could be achieved using 4.0Mn-CN as the catalyst. PCN could not remove OA neither in a Vis/O₂ nor O₃ system, which indicated that PCN photocatalysis and PCN catalytic ozonation can hardly produce •OH. 4.0Mn-CN exhibited negligible activity in the Vis/O₂ system, but 40.6% of OA was degraded within 60 min in the 4.0Mn-CN/O₃ system, indicating Mn single atoms act as the active sites for O₃ activation. It is worth noting that the performance of 4.0Mn-CN in photocatalytic ozonation is still higher than that of PCN, after deducting the contribution of the catalytic ozonation pathway.

Considering that O₃ was the main source for •OH generation, O₃ decomposition rates over different catalysts were conducted. A faster decomposition rate of O₃ was observed in the PCN/Vis/O₃ system than that in the PCN/O₃ system (Fig. 2b), but it is slower than that in the 4.0Mn-CN/Vis/O₃. This is in agreement with the degradation results. Surprisingly, 4.0Mn-CN performed a similar ozone decomposition rate

in the Vis/O₃ system to that in O₃ system, but the rate constant of OA removal in the former system (4.2×10^{-2} mmol·(L·min)⁻¹) is 3 times greater than that in the latter one (1.4×10^{-2} mmol·(L·min)⁻¹). This indicated distinct reaction pathways in the 4.0Mn-CN/Vis/O₃ system, which leads to a higher utilization efficiency of O₃ than the 4.0Mn-CN/O₃ system. Furthermore, a wide array of organic pollutants was selected to evaluate the degradation ability of 4.0Mn-CN/Vis/O₃ system, such as bisphenol A (BPA), p-nitrophenol (PNP), p-benzoquinone (PBQ) and benzoic acid (BA). As it was shown, 4.0Mn-CN exhibited remarkable activity in total organic carbon mineralization within 90 min (Fig. 2c), suggesting its great potential in treatment of different organic contaminants in wastewater. Furthermore, we compared the performance of 4.0Mn-CN with other catalysts reported in previous studies. 4.0Mn-CN exhibits better performance than other reported materials, such as WO₃, UCN, and GCN supported ZnO and NiO catalysts, in photocatalytic

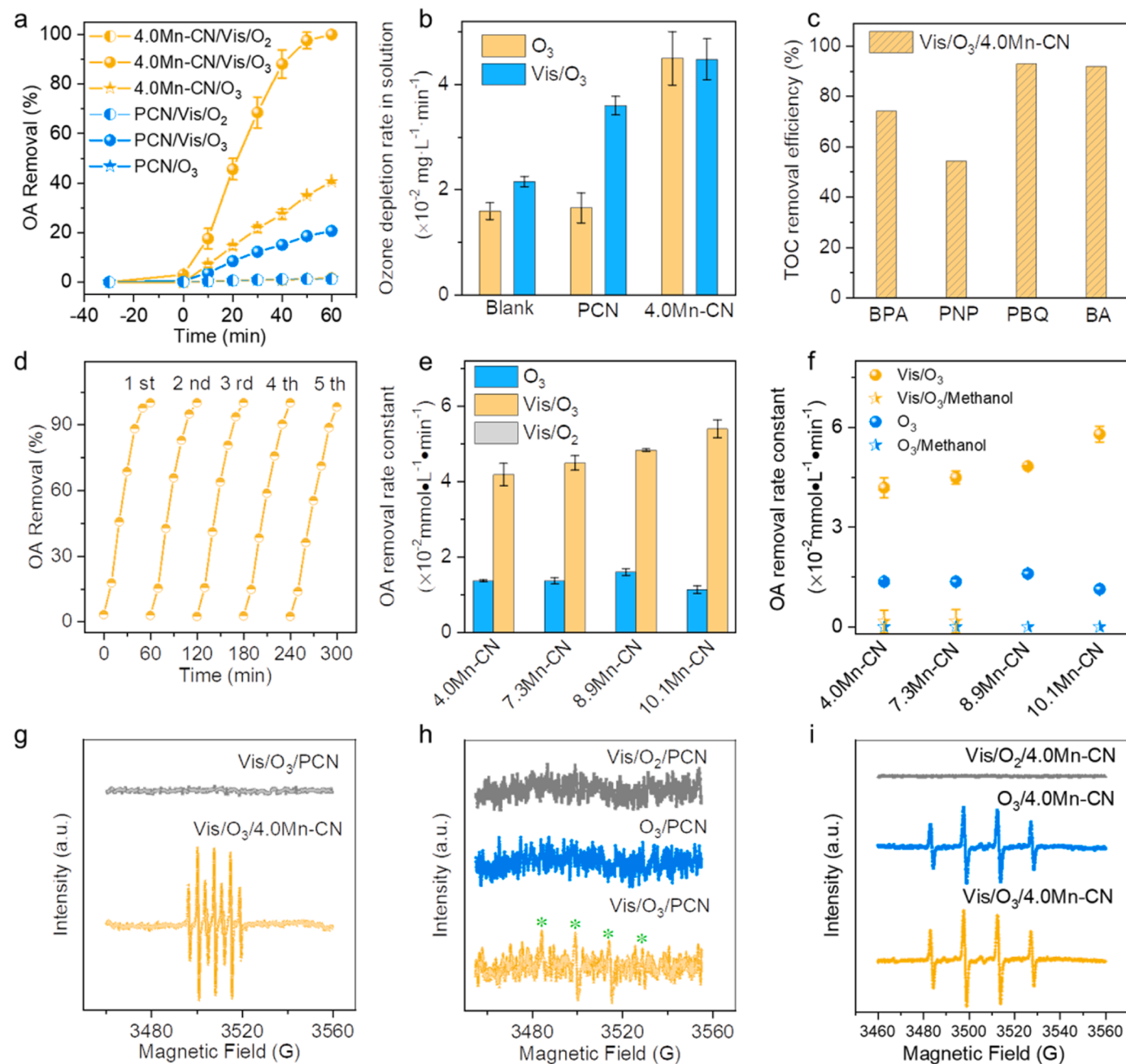


Fig. 2. Degradation curves of OA in ozonation, photocatalytic oxidation and photocatalytic ozonation with PCN or 4.0Mn-CN (a). Corresponding O₃ decay curves in ozonation and photocatalytic ozonation with or without catalysts (b). TOC removal efficiency of BPA, PNP, PBQ and BA in photocatalytic ozonation with 4.0Mn-CN (BPA/PNP/PBQ/BA: 50 mg/L) (c). Catalytic stability of 4.0Mn-CN in successive cycling tests (d). OA removal rate constants in ozonation and photocatalytic ozonation with different Mn-CNs (e). The quenching tests by methanol in ozonation and photocatalytic ozonation processes for all Mn-CNs (f). EPR spectra of DMPO-•OH adduct in photocatalytic ozonation process with PCN and 4.0Mn-CN at a DMPO concentration of 0.2 mM (g). EPR spectra of the DMPO-•OH adduct in ozonation, photocatalytic oxidation and photocatalytic ozonation processes at a DMPO concentration of 0.6 mM: PCN (h); 4.0Mn-CN (i).

ozonation of organic pollutants (Table S3) [7,42–44]. Thus, carbon nitride supported Mn SACs demonstrate the advantage.

The removal rate of OA over a repetitive use was monitored to evaluate the catalytic stability of 4.0Mn-CN. After each test, the catalyst was collected by vacuum filtration, washed three times with ultrapure water, and dried overnight at 80 °C. As shown in Fig. 2d, the performance of 4.0Mn-CN remained relatively constant over 5 cycles of reuse. Meanwhile, the Mn leaching during catalyst recycling was also recorded (Figure S10), and the concentration is less than 0.17 mg/L. The little leaching of Mn is consistent with its stable catalytic activity. The XANES spectra of the tested 4.0Mn-CN (Figure S11) show no peak of metallic

Mn–Mn bond but the main peak corresponding to the Mn–N bond, which suggests that Mn maintains in a single atom state after 5 h test. The negligible change in the C K-edge and N K-edge spectra of the used 4.0Mn-CN (Figure S12) further confirmed its good stability.

Upon increasing the Mn content, the removal rate constant of OA was further improved in the Mn-CN/Vis/O₃ system (Fig. 2e). In particular, 10.1Mn-CN achieved a rate constant of $5.4 \times 10^{-2} \text{ mmol} \cdot (\text{L} \cdot \text{min})^{-1}$, which was 1.3 times and 7.7 times greater than those of 4.0Mn-CN and PCN, respectively. However, the mass activity of Mn-CN calculated using actual mass loading of Mn decreased with the increasing loading of Mn (Figure S13). The rate of 4.0Mn-CN ($3.5 \text{ mmol} \cdot (\text{L} \cdot \text{min} \cdot \text{mg}_{\text{Mn}})^{-1}$) was

almost 2 times greater than that of 10.1Mn-CN (1.8 mmol·(L·min·mg_{Mn})⁻¹). Interestingly, a positive correlation between OA removal rate constant in Vis/O₃ system with the surface area of Mn-CN samples was observed (Figure S14a). It is obvious that the high surface area benefits the participation of more active sites in surface reaction. However, the concentration of surface charge carriers is the crucial aspect for the photocatalytic activity [45]. Consequently, there is no clear relationship between OA removal rate constant with the surface area of catalysts when the PCN is included (Figure S14b). Meanwhile, the Mn content not only regulates the active site density, but also affects the supply of photogenerated electrons by changing the band structure,

separation and transport of charge carriers. The effects would lead to a trade-off in performance. Additionally, the concentration of surface Mn atoms tends to saturate in the Mn-CN samples with a high content of Mn, and some single atoms exist in the interlayer of carbon nitride and cannot participate in surface reactions. Therefore, these factors may significantly lower the mass activity of Mn-CN at high density of Mn single atoms.

Radical quenching experiments were conducted to identify the active species generated during O₃ activation with or without visible light. Methanol was added as a scavenger for ·OH, which can completely inhibit the removal of OA in both photocatalytic ozonation and catalytic

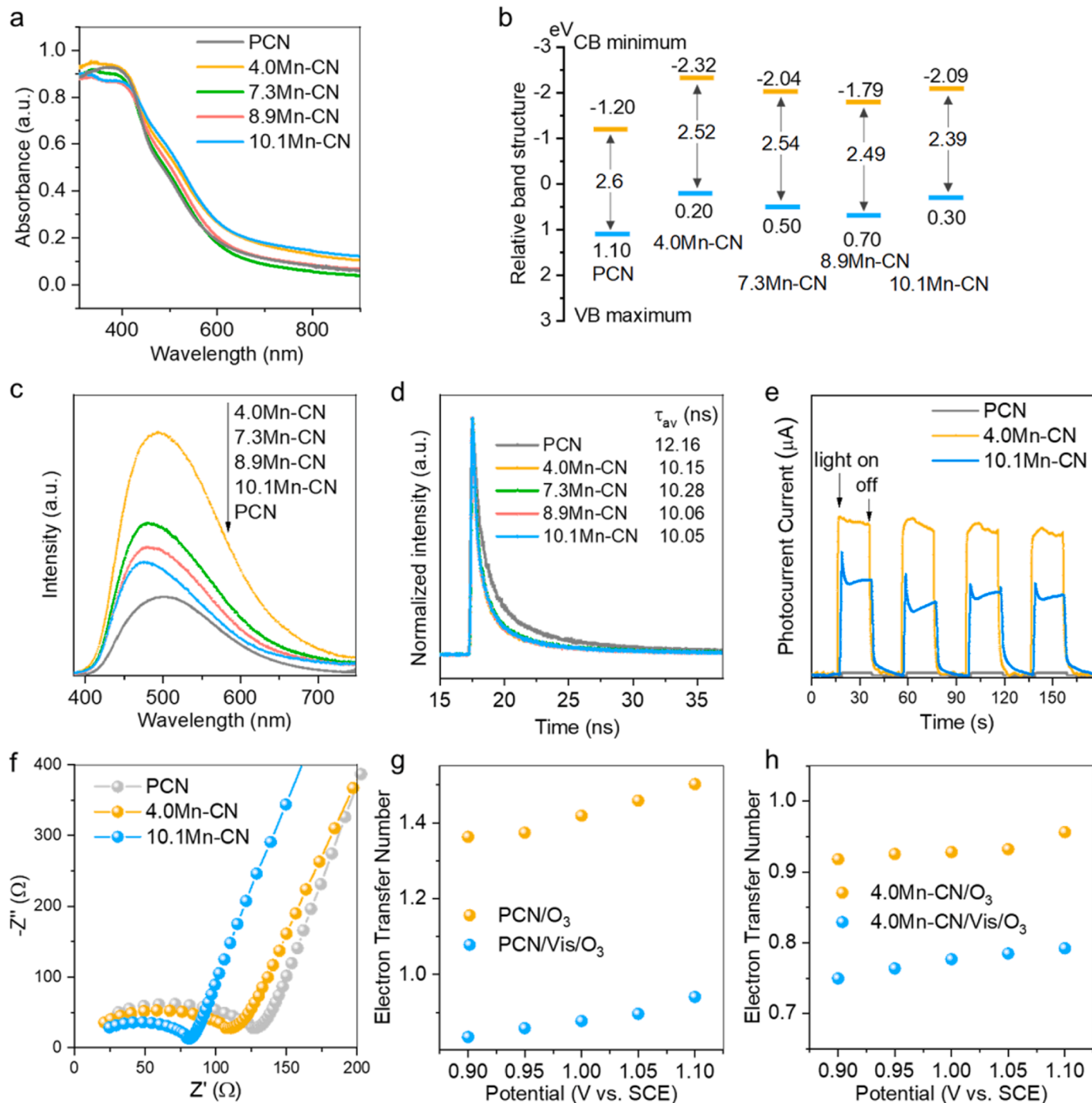


Fig. 3. UV–Vis absorption spectra (a); Plots of band structure (b); Steady-state PL (c); Time-resolved PL decay spectra of all samples (excitation at 330 nm) (d); Photoelectrochemical tests of PCN, 4.0Mn-CN and 10.1Mn-CN (e); Electrochemical impedance spectroscopy (EIS) measurements of PCN, 4.0Mn-CN and 10.1Mn-CN (f); The electron transfer number under O₃ or solar/O₃ treatment on PCN (h); 4.0Mn-CN (i).

ozonation with all Mn-CNs (Fig. 3f), thus $\cdot\text{OH}$ was the dominant active species for OA degradation [46]. EPR was employed to further identify the formation of $\cdot\text{OH}$. At a 5,5-dimethyl-1-pyrroline N-oxide (DMPO) concentration of 0.2 mM, a characteristic signal with an intensity ratio of 1:2:1:2:1:2:1 was observed in 4.0Mn-CN/O₃ system, which can be assigned to 5,5-dimethyl-1-pyrrolidone-2-oxyl (DMPOX) [47]. Meanwhile, this signal cannot form in an ozonation or PCN/O₃ system (Fig. 2g). This result indicates that the presence of Mn single atoms can enhance the concentration of O₃ in aqueous solution, because DMPO can be directly oxidized to DMPOX when the ozone concentration in solution is high [48]. Then the concentration of DMPO was increased to 0.6 mM to eliminate the interference of dissolved ozone. As expected, a characteristic quartet of signals assigned to the DMPO- $\cdot\text{OH}$ adduct was detected in all catalytic systems with the presence of O₃, rather than O₂ under visible light (Figs. 2h and 2i) [47]. It confirms that the generation of $\cdot\text{OH}$ arises from the decomposition of O₃ rather than O₂. Compared with catalytic ozonation, intensively enhanced EPR signals were observed in both PCN/Vis/O₃ and 4.0Mn-CN/Vis/O₃ systems, which further confirms that visible light irradiation can evidently improve the yield of $\cdot\text{OH}$ generation. Meanwhile, the higher signal intensity over the Mn-CN than that of PCN is consistent to their photocatalytic performance.

3.3. Light-harvesting and charge transfer dynamics

According to UV-Vis absorption (Fig. 3a) and the corresponding Tauc plots (Figure S15a), PCN exhibited an absorption edge at around 470 nm (2.60 eV), and the introduction of Mn species slightly narrowed the band gap (2.39–2.52 eV). An improved light absorbance was also observed on Mn-CNs, and no intermediate states were generated in their bandgap. Combining with the XPS valence band spectra (Figure S15b), the detailed band positions for each sample are obtained and summarized in Fig. 3b. The loading of Mn resulted in the narrow bandgap by up-shifting both the valence band (VB) maximum and the conduction band (CB) minimum. This is because of the hybridization of Mn 4d with N 2p orbital and charge transfer between Mn and PCN support. [36] The higher position of the CB minimum in Mn-CN than PCN indicates a greater reduction ability of photogenerated electrons, which is consistent with its activity trend (Fig. 2e). It is noted that the increased concentration of Mn shifts the VB maximum and CB minimum up and then down. This is probably associated with the trade-off between Mn and melem-Mn concentration because an excessive Mn content suppresses the polymerization process from melem to carbon nitride, as indicated by XRD results [36,37]. Consequently, an increase of Mn content will lead to a narrower band gap, as well as a slight downward shift of CB, which promotes the utilization of reactive carriers for $\cdot\text{OH}$ generation.

The charge separation and recombination processes were probed by measuring the steady-state PL spectra [49]. As shown in Fig. 3c, an evident emission signal attributable to the band-edge emission at \sim 520 nm was observed on PCN. By comparison, the PL intensity of 4.0Mn-CN substantially increased by approximately 3 times compared to PCN. In addition, blue-shifted PL peaks with smaller Stokes shifts and broadened widths occurred, which can be assigned to the exciton-related radiation [49,50]. This result indicates that the incorporation of Mn single atoms may bring in new trap states to accumulate carriers, and the high concentration of localized excitons around Mn sites leads to an obviously increased fluorescence. As the loading of Mn increases, the PL intensity gradually weakens and blue shifts, but it is still stronger than that of the metal-free PCN. The lower PL intensity is due to the reduced inter-band radiative recombination of photoexcited carriers with the increasing content of Mn. The blue-shifted PL peaks over Mn-CNs can be ascribed to the quantum confinement induced by the reduced layer stacking thickness due to the appearance of the uncondensed melem [37,49]. Nanosecond time-resolved PL was also conducted to study the charge carrier kinetics in various samples (Fig. 3d and Table S4) [49,51]. The accelerated PL decay kinetics was

observed on Mn-CN compared with PCN, and an average lifetime of PCN and 4.0Mn-CN are 12.16 and around 10.15 ns, respectively, likely because that the formation of Mn-N bond among the tri-s-triazine ring enhanced the charge separation.

The photo-electro-chemical test shows that the loading of Mn can greatly enhance the photocurrent density (Fig. 3e). The photocurrent over 4.0Mn-CN is at a 56.2-fold increase compared with that of PCN, because the formation of Mn-N bond can facilitate charge transfer. Surprisingly, the photocurrent density of 10.1Mn-CN with better catalytic activity is lower than that of 4.0Mn-CN. It is noteworthy that a higher metal loading in 10.1Mn-CN causes a more impact on the polymerization process from melem to carbon nitride, and a low crystallinity is detrimental to intra-layer and inter-layer charge transfer [52]. For Mn-CNs, the tri-s-triazine ring serves as the dominant light-harvesting unit, and the formation of Mn-N bond can ensure the rapid movement of charge carriers to the adjacent Mn single atoms. Thus, the increased Mn single-atom density shortens the transfer distance of charge carriers, guaranteeing the capture of electrons by O₃ molecules timely. Consequently, 10.1Mn-CN behaves more actively than 4.0Mn-CN. Moreover, the EIS measurements were conducted (Fig. 3f). The smaller arc radius on 4.0Mn-CN than PCN indicates that Mn single atoms can lower the interfacial charge transfer resistance, improving the mobility of photo-generated electrons. In situ-electrochemical measurements showed that the numbers of electron transfer of PCN and 4.0Mn-CN are close to 1 under visible light (Figs. 3g and 3h), from the Koutecky–Levich (K–L) plots (Figure S16-17), confirming the one-electron-reduction route in the Vis/O₃ system. In addition, the electron transfer number of 4.0Mn-CN is lower than that of PCN, presumably because Mn single-atom active sites can accelerate the interfacial delivery of photoexcited electrons to react with O₃ molecules.

The charge carrier dynamics at the picosecond time scale was monitored by femtosecond transient absorption (TA) spectroscopy. Upon photoexcitation (400 nm) of PCN, 4.0Mn-CN, and 10.1Mn-CN in vacuum, the intuitive pseudo-color TA spectra for all the samples act as a function of delay time and probe wavelength (3000–8000 nm) to observe TA kinetics. A similar evolution of spectral profiles with a photoinduced absorption feature centered at around 3000 nm was observed in all the TA spectra (Fig. 4a-c). Fig. 4d-f show TA kinetic plots of PCN, 4.0Mn-CN and 10.1Mn-CN probed at 3500 nm for the deeply trapped electrons and/or holes, fitted using a bi-exponential equation [21,53]. The fitting results by the bi-exponential decay functions are $\tau_1=5.58$ ps (19%), $\tau_2=144.5$ ps (29%) and $\tau_3=4712$ ps (49%) for PCN, $\tau_1=3.0$ ps (37%), $\tau_2=89.4$ ps (32%) and $\tau_3=5341$ ps (26%) for 4.0Mn-CN, and $\tau_1=1.1$ ps (53%), $\tau_2=28.7$ ps (25%) and $\tau_3=2640$ ps (22%) for 10.1Mn-CN. The robust increase for τ_1 ascribed to the electrons transfer to shallow trapping state is strongly correlated with the content of Mn as compared with PCN [54]. This result indicates that a new trap state arising from Mn loading can capture electrons, which offers more opportunities for electrons to reduce O₃, because MnN₄ also serves as the reaction center in the one-electron-reduction route. Meanwhile, the formation of Mn-N bond constructs a channel for the transfer of charge carriers, and the oriented transfer with a short distance for the reaction between electrons and O₃ greatly improve the yield of $\cdot\text{OH}$.

3.4. DFT calculations

To gain the insight into the impact of Mn single atoms on the photocatalytic process in detail, we performed DFT calculations. The O₃ adsorption on PCN is evidently weak with adsorption energy of 0.16 eV, and the optimized distance between O₃ and the melon plane is too far to achieve efficient electron transfer (Figure S18). By comparison, an exothermic process of O₃ adsorption on the MnN₄ site of a Mn-CN catalyst is observed, with large adsorption energy of \sim 2.15 eV (Fig. 5a). In such a case, the elongated O-O bond of O₃ facilitates its subsequent reduction by photoelectrons [55]. Therefore, the anchor of

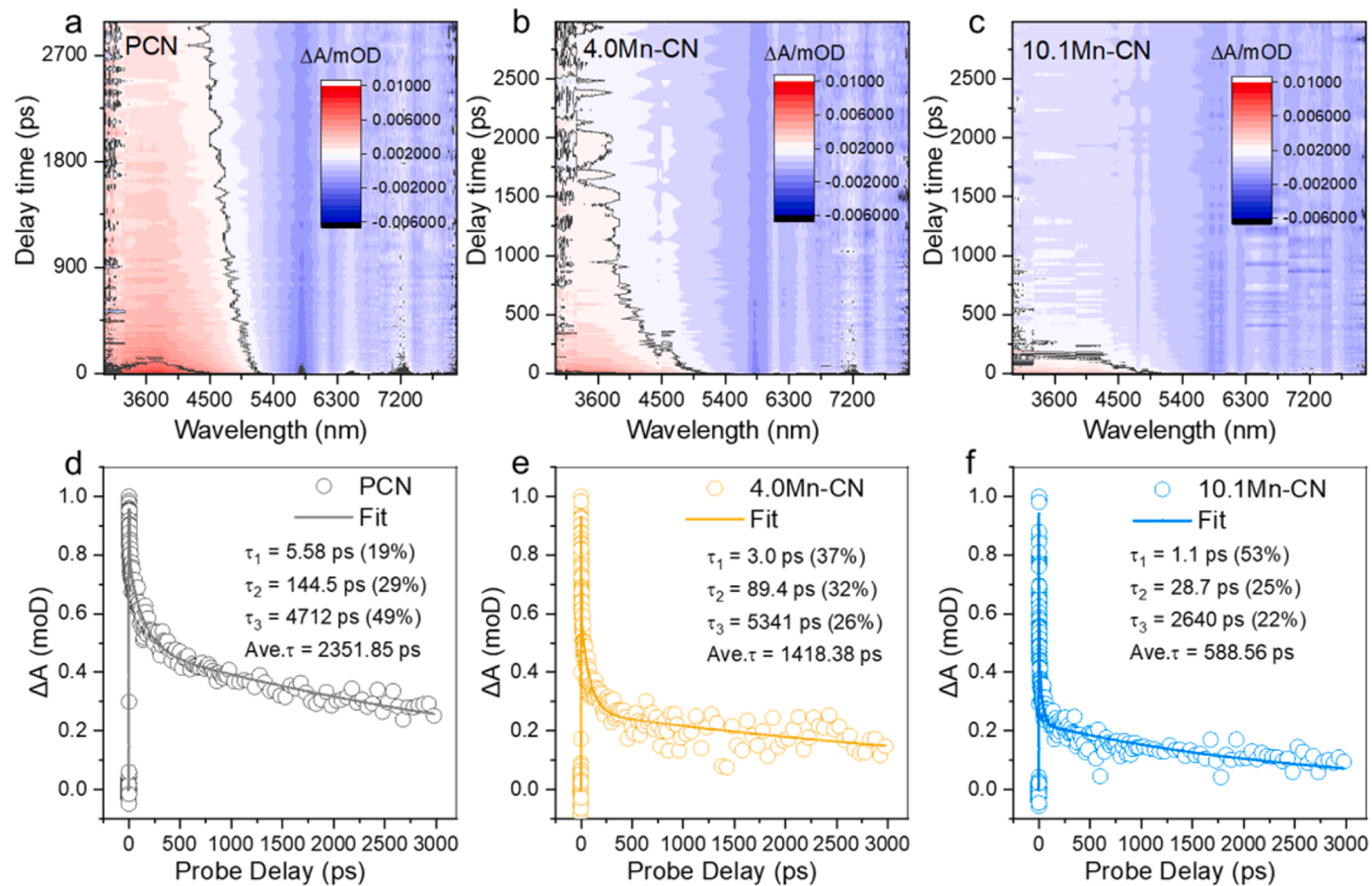


Fig. 4. Pseudo fs-TA spectra of PCN (a), 4.0Mn-CN (b) and 10.1Mn-CN (c) at the probe wavelength of 3000–8000 nm (excited at 400 nm). TA kinetic plots and typical fitting curves of PCN (d), 4.0Mn-CN (e) and 10.1Mn-CN (f) probed at 3500 nm.

Mn single atoms on carbon nitride can optimize the adsorption and activation of O_3 .

From the density of state (DOS) analysis, Mn single atoms can expand the light absorption range of PCN by narrowing the band gap, rather than introducing an impurity level (Fig. 5b and S19). This is in agreement with the result of the band structure revealed by UV-Vis absorption and XPS. Significantly, the formation of MnN_4 configuration causes an obviously enhanced DOS at the Fermi level. This implies that the introduction of Mn single atoms can improve the conductivity of the catalyst and facilitate the photo-excited electron transfer to the catalyst surface, which is consistent with EIS results [56]. It should be noted that this molecular orbital exhibits a slightly higher energetic level than the molecular orbitals contributed by N and C, evidenced by the greatly shifted CB minimum of Mn-CN. Fig. 5c shows the lowest unoccupied molecular orbital (LUMO) locations of PCN and Mn-CN. The density of electronic states uniformly distributes in tri-s-triazine units of PCN. By comparison, a large number of excited charge carriers are concentrated at Mn atoms, suggesting that the anchor of Mn single atoms on carbon nitride can promote the excitation and transfer of photo-excited electrons.

Based on the above discussions, the mechanism of enhanced generation of $^{\bullet}OH$ in Mn-CN photocatalytic ozonation is proposed as follows (Fig. 6). The Mn single atoms on carbon nitride promotes the excitation and transfer of photo-generated electrons, and thus increases the number of available photo-generated electrons. The formation of localized charge carriers around Mn atoms after light irradiation narrows the migration distance of the electrons for surface reactions, enriching the number of available photo-generated electrons. Meanwhile, a fast one-electron-reduction reaction kinetics increases the utilization of surviving charge carriers due to the bifunctional role of Mn single atoms as

adsorption and catalytic sites for O_3 . We previously found that electron reduction (one $^{\bullet}OH$ only consumes one O_3) and catalytic ozonation (one $^{\bullet}OH$ may need to consume more than one O_3) for the generation of $^{\bullet}OH$ from O_3 occur at different active sites of Co single-atom catalysts, showing two paths [57,58]. However, these two paths share the same active site on Mn-CN, and the light irradiation favors the selectivity of the electron-reduction path. Therefore, Mn single atoms significantly improved the photocatalytic ozonation performance by achieving high utilization efficiency of both electrons and O_3 .

4. Conclusion

In this work, we reported a highly active Mn single atom catalyst supported on PCN (Mn-CN) for $^{\bullet}OH$ generation via ozone activation under visible light irradiation. The anchor of Mn single atoms on carbon nitride promotes the excitation and transfer of photo-generated electrons and creates a high concentration of localized charge carriers around the MnN_4 sites. The preferential adsorption of O_3 on the MnN_4 sites favors fast one-electron-reduction reaction kinetics and the enriched O_3 and electrons around the MnN_4 sites greatly enhance the utilization of photogenerated electrons for the generation of $^{\bullet}OH$. Importantly, the regulation of Mn single atoms density can manipulate the trade-off between the number of available electrons and active sites in photocatalytic performance. As a result, the Mn-CN catalyst manifests a remarkable enhancement in the OA degradation, and other organic pollutants are also effectively mineralized. This work opens up a strategy for designing excellent SACs for organic wastewater remediation by photocatalytic ozonation and provides a new insight to the mechanism.

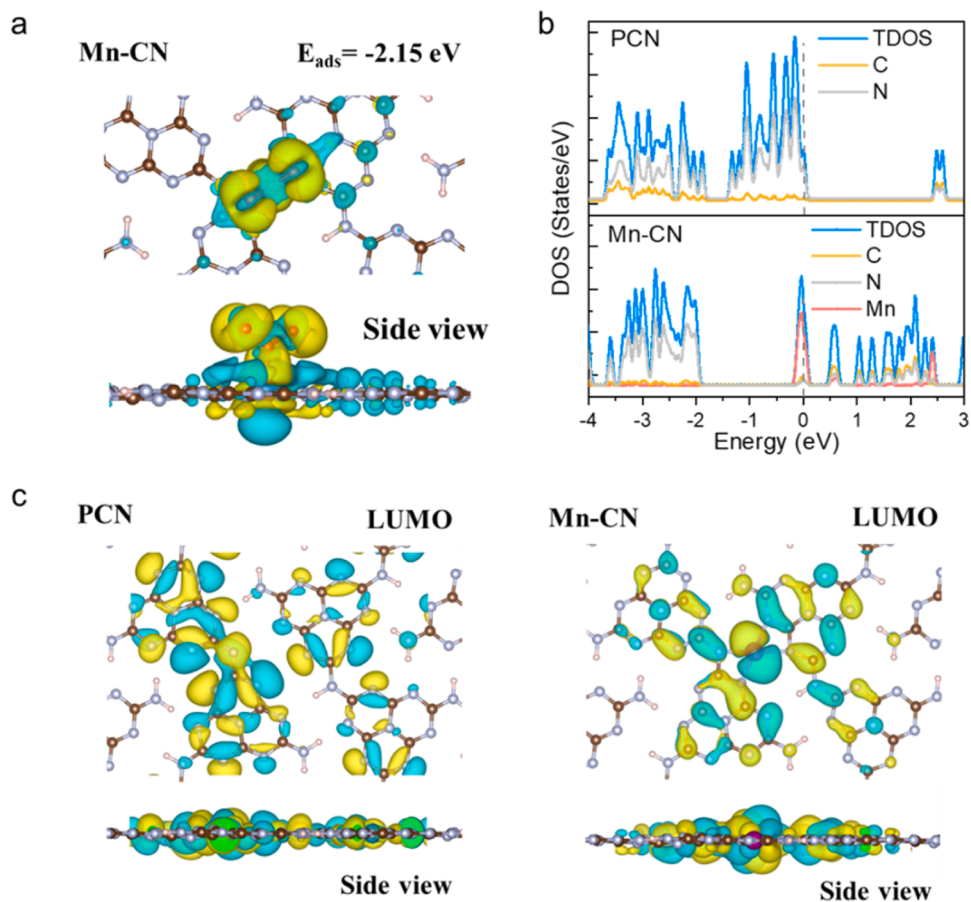


Fig. 5. Different charge densities for O_3 adsorption on Mn-CN (a); DOS of PCN and Mn-CN (b); Charge distributions of LUMO of PCN and Mn-CN (c). The electron accumulation and depletion at an iso-surface value of 0.001 \AA^{-3} are shown in the colors of yellow and blue, respectively. The brown, gray, red and purple colors represent carbon, nitrogen, oxygen and manganese, respectively.

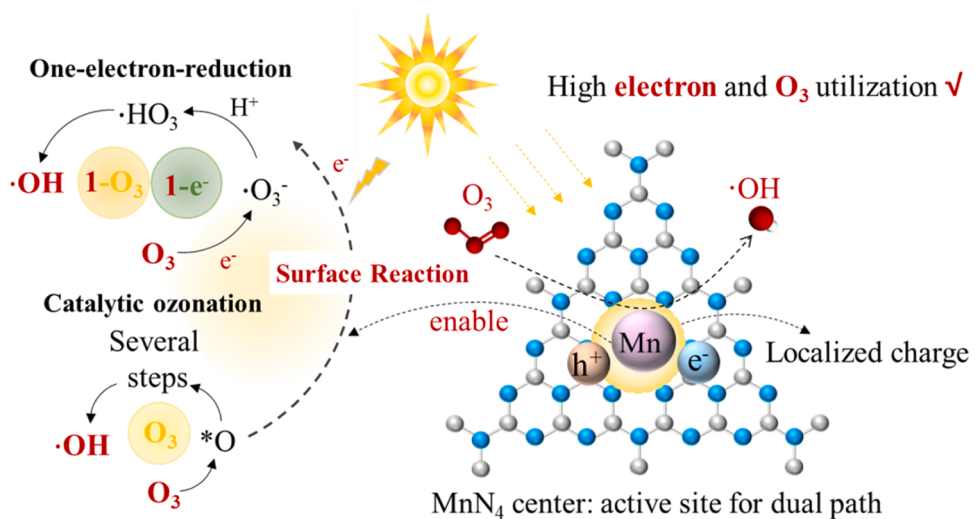


Fig. 6. Illustration of the reaction mechanism of Mn-CN in photocatalytic ozonation system.

CRediT authorship contribution statement

Jing Wang: Writing – review & editing, Writing – original draft, Visualization, Investigation, Formal analysis, Data curation, Conceptualization. **Shaobin Wang:** Writing – review & editing, Validation. **Yongbing Xie:** Writing – review & editing, Validation, Supervision, Conceptualization. **Zhuan Wang:** Methodology, Funding acquisition.

Yuxian Wang: Methodology, Funding acquisition. **Yuxiang Weng:** Methodology. **Hongbin Cao:** Supervision, Resources, Funding acquisition. **Zhaomeng Xu:** Validation, Investigation. **Yanjun Xu:** Investigation, Data curation. **Shenning Liu:** Investigation, Data curation. **Jiakai Qiu:** Validation.

Declaration of Competing Interest

The authors declare that they have no known competing financial interests or personal relationships that could have appeared to influence the work reported in this paper.

Data Availability

Data will be made available on request.

Acknowledgements

This work is financially supported by the National Natural Science Foundation of China (51934006), Science Foundation of China University of Petroleum, Beijing (2462021QNXZ009) and the strategic priority research program of the Chinese Academy of Sciences (XDB33000000). The synchrotron tests were performed at Beijing Synchrotron Radiation Facility under the support of 4B9A beamline.

Appendix A. Supporting information

Supplementary data associated with this article can be found in the online version at [doi:10.1016/j.apcatb.2024.123900](https://doi.org/10.1016/j.apcatb.2024.123900).

References

- [1] S. Loeb, P. Alvarez, J. Brame, E. Cates, W. Choi, J. Crittenden, D. Dionysiou, Q. Li, G. Li-Puma, X. Quan, D. Sedlak, T. David Waite, P. Westerhoff, J. Kim, The technology horizon for photocatalytic water treatment: sunrise or sunset? *Environ. Sci. Technol.* 53 (2019) 2937–2947.
- [2] A. Kumar, A. Kumar, V. Krishnan, Perovskite oxide based materials for energy and environment-oriented photocatalysis, *ACS Catal.* 20 (2020) 10253–10315.
- [3] Y. Wang, J. Sheng, X. Zhao, Y. He, F. Dong, Y. Sun, Boosted photocatalytic efficiency of QDs sensitized $(\text{BiO})_2\text{CO}_3/\beta\text{-Bi}_2\text{O}_3$ heterojunction via enhanced interfacial charge transfer, *Chin. Chem. Lett.* 34 (2023) 107967.
- [4] W. Koppenol, D. Stanbury, P. Bounds, Electrode potentials of partially reduced oxygen species, from dioxygen to water, *Free Radic. Biol. Med.* 49 (2010) 317–322.
- [5] C. Gao, J. Low, R. Long, T. Kong, J. Zhu, Y. Xiong, Heterogeneous single-atom photocatalysts: fundamentals and applications, *Chem. Rev.* 120 (2020) 12175–12216.
- [6] H. Kim, H. Kim, S. Weon, G. Moon, J. Kim, W. Choi, Co-catalytic performance of nanodiamonds loaded on wo_3 for the decomposition of volatile organic compounds under visible light, *ACS Catal.* 6 (2016) 8350–8360.
- [7] Y. Wang, X. Li, S. Liu, Y. Liu, T. Kong, H. Zhang, X. Duan, C. Chen, S. Wang, Roles of catalyst structure and gas surface reaction in the generation of hydroxyl radicals for photocatalytic oxidation, *ACS Catal.* 12 (2022) 2770–2780.
- [8] C. Wang, T. Zhang, W. Yu, R. Si, Y. Liu, Z. Zhao, Modulating location of single copper atoms in polymeric carbon nitride for enhanced photoredox catalysis, *ACS Catal.* 10 (2020) 5715–5722.
- [9] J. Xiao, J. Rabeah, J. Yang, Y. Xie, H. Cao, A. Brückner, Fast electron transfer and OH^- formation key features for high activity in visible-light-driven ozonation with C_3N_4 catalysts, *ACS Catal.* 7 (2017) 6198–6206.
- [10] H. Cao, J. Wang, J. Kim, Z. Guo, J. Xiao, J. Yang, J. Chang, Y. Shi, Y. Xie, Different roles of Fe atoms and nanoparticles on $\text{g-C}_3\text{N}_4$ in regulating the reductive activation of ozone under visible light, *Appl. Catal. B* 296 (2021) 120362.
- [11] J. Wang, T. Heil, B. Zhu, C. Tung, J. Yu, G. Chen, M. Antonietti, S. Cao, A. Single, Single Cu-center containing enzyme-mimic enabling full photosynthesis under CO_2 reduction, *ACS Nano* 14 (2020) 8584–8593.
- [12] Y. Li, B. Li, D. Zhang, L. Cheng, Q. Xiang, Crystalline carbon nitride supported copper single atoms for photocatalytic CO_2 reduction with nearly 100% CO selectivity, *ACS Nano* 14 (2020) 10552–10561.
- [13] M. Ren, X. Zhang, Y. Liu, G. Yang, L. Qin, J. Meng, Y. Guo, Y. Yang, Interlayer palladium-single-atom-coordinated cyano-group-rich graphitic carbon nitride for enhanced photocatalytic hydrogen production performance, *ACS Catal.* 12 (2022) 5077–5093.
- [14] Y. Zhao, J. Guo, Z. Yang, L. Li, J. Cui, P. Zhang, C. Hu, C. Diao, W. Choi, Efficient exciton dissociation in ionically interacted methyl viologen and polymeric carbon nitride for superior H_2O_2 photoproduction, *ACS Catal.* 13 (2023) 2790–2801.
- [15] Z. Teng, H. Yang, Q. Zhang, O. Teruhisa, Carrier dynamics and surface reaction boosted by polymer-based single-atom photocatalysts, *Chem. Res. Chin. Univ.* 38 (2022) 1207–1218.
- [16] C. Bie, L. Wang, J. Yu, Challenges for photocatalytic overall water splitting, *Chem* 8 (2022) 1567–1574.
- [17] B. Qiao, A. Wang, X. Yang, L. Allard, Z. Jiang, Y. Cui, J. Liu, J. Li, T. Zhang, Single-atom catalysis of CO oxidation using Pt_1/FeO_x , *Nat. Chem.* 3 (2011) 634–641.
- [18] A. Wang, J. Li, T. Zhang, Heterogeneous single-atom catalysis, *Nat. Rev. Chem.* 2 (2018) 65–81.
- [19] X. Chen, X. Zhao, Z. Kong, W. Ong, N. Li, Unravelling the electrochemical mechanisms for nitrogen fixation on single transition metal atoms embedded in defective graphitic carbon nitride, *J. Mater. Chem. A* 6 (2018) 21941.
- [20] P. Zhou, M. Luo, S. Guo, Optimizing the semiconductor-metal-single-atom interaction for photocatalytic reactivity, *Nat. Rev. Chem.* 6 (2022) 823–838.
- [21] H. Fei, J. Dong, Y. Feng, C. Allen, C. Wan, B. Voloskiy, M. Li, Z. Zhao, H. Sun, P. An, W. Chen, Z. Guo, C. Lee, D. Chen, I. Shakir, M. Liu, T. Hu, Y. Li, A. Kirkland, X. Duan, Y. Huang, General synthesis and definitive structural identification of Mn_4C_4 single-atom catalysts with tunable electrocatalytic activities, *Nat. Catal.* 1 (2018) 63, 27.
- [22] D. Huang, N. He, Q. Zhu, C. Chu, S. Weon, K. Rigby, X. Zhou, L. Xu, J. Niu, E. Stavitski, J. Kim, Conflicting roles of coordination number on catalytic performance of single-atom Pt catalysts, *ACS Catal.* 11 (2021) 5586–5592.
- [23] Y. Shi, Y. Zhou, Y. Lou, Z. Chen, H. Xiong, Y. Zhu, Homogeneity of supported single-atom active sites boosting the selective catalytic transformations, *Adv. Sci.* 9 (2022) 2201520.
- [24] X. Fang, Q. Shang, Y. Wang, L. Jiao, T. Yao, Y. Li, Q. Zhang, Y. Luo, H. Jiang, Single Pt atoms confined into a metal-organic framework for efficient photocatalysis, *Adv. Mater.* 30 (2018) 1705112.
- [25] W. Jiang, Y. Zhao, X. Zong, H. Nie, L. Niu, L. An, D. Qu, X. Wang, Z. Kang, Z. Sun, Photocatalysis for high-performance H_2 production: Ga-doped polymeric carbon nitride, *Angew. Chem. Int. Ed.* 60 (2021) 6124–6129.
- [26] Z. Teng, Q. Zhang, H. Yang, K. Kato, W. Yang, Y. Lu, S. Liu, C. Wang, A. Yamakata, C. Su, B. Liu, T. Ohno, Atomically dispersed antimony on carbon nitride for the artificial photosynthesis of hydrogen peroxide, *Nat. Catal.* 4 (2021) 374–384.
- [27] L. Su, P. Wang, X. Ma, J. Wang, S. Zhan, Regulating local electron density of iron single sites by introducing nitrogen vacancies for efficient photo-fenton process, *Angew. Chem. Int. Ed.* 60 (2021) 21261–21266.
- [28] Z. Guo, Y. Xie, J. Xiao, J. Zhao, Y. Wang, Z. Xu, Y. Zhang, L. Yin, H. Cao, J. Gong, Single-atom $\text{Mn}-\text{N}_4$ site-catalyzed peroxone reaction for the efficient production of hydroxyl radicals in an acidic solution, *J. Am. Chem. Soc.* 141 (2019) 12005–12010.
- [29] H. Bader, J. Hoigné, Determination of ozone in water by the indigo method, *Water Res.* 15 (4) 449–456.
- [30] G. Kresse, J. Furthmüller, Efficiency of ab-initio total energy calculations for metals and semiconductors using a plane-wave basis set, *Comput. Mater. Sci.* 6 (1996) 15–50.
- [31] G. Kresse, J. Furthmüller, Efficient iterative schemes for ab initio total-energy calculations using a plane-wave basis set, *Phys. Rev. B* 54 (1996) 11169–11186.
- [32] J. Perdew, K. Burke, M. Ernzerhof, Generalized gradient approximation made simple, *Phys. Rev. Lett.* 77 (1996) 3865–3868.
- [33] G. Kresse, D. Joubert, From ultrasoft pseudopotentials to the projector augmented-wave method, *Phys. Rev. B* 59 (1999) 1758–1775.
- [34] P. Blöchl, Projector augmented-wave method, *Phys. Rev. B* 50 (1994) 17953–17979.
- [35] S. Grimme, J. Antony, S. Ehrlich, H. Krieg, A consistent and accurate ab initio parametrization of density functional dispersion correction (DFT-D) for the 94 elements H–Pu, *J. Chem. Phys.* 132 (2010) 154104.
- [36] X. Wang, K. Maeda, A. Thomas, K. Taka-nabe, G. Xin, J. Carlsson, K. Domen, M. Antonietti, A metal-free polymeric photocatalyst for hydrogen production from water under visible light, *Nat. Mater.* 8 (2009) 76–80.
- [37] Y. Li, Z. Wang, T. Xia, H. Ju, K. Zhang, R. Long, Q. Xu, C. Wang, L. Song, J. Zhu, J. Jiang, Y. Xiong, Implementing metal-to-ligand charge transfer in organic semiconductor for improved visible-near-infrared photocatalysis, *Adv. Mater.* 28 (2016) 6959–6965.
- [38] A. Thomas, A. Fischer, F. Goettmann, M. Antonietti, J. Müller, R. Schlogl, J. Carlsson, Graphitic carbon nitride materials: variation of structure and morphology and their use as metal-free catalysts, *J. Mater. Chem.* 18 (2008) 4893–4908.
- [39] L. Yang, J. Huang, L. Shi, L. Cao, Y. Jie, H. Ouyang, J. Ye, A surface modification resultant thermally oxidized porous $\text{g-C}_3\text{N}_4$ with enhanced photocatalytic hydrogen production, *Appl. Catal. B* 20 (2017) 335–345.
- [40] W. Wang, H. Zhang, S. Zhang, Y. Liu, G. Wang, C. Sun, H. Zhao, Potassium-ion-assisted regeneration of active cyano groups in carbon nitride nanoribbons: visible-light-driven photocatalytic nitrogen reduction, *Angew. Chem. Int. Ed.* 58 (2019) 16644–16650.
- [41] P. Faria, J. Orfao, M. Pereira, Activated carbon catalytic ozonation of oxamic and oxalic acids, *Appl. Catal. B* 79 (2008) 237–243.
- [42] H. Yu, M. Wang, J. Yan, H. Dang, H. Zhu, Y. Liu, M. Chen, G. Li, L. Wu, Complete mineralization of phenolic compounds in visible-light-driven photocatalytic ozonation with single-crystal WO_3 nanosheets: Performance and mechanism investigation, *J. Hazard. Mater.* 433 (2022) 128811.
- [43] X. Yuan, S. Duan, G. Wu, L. Sun, G. Cao, D. Li, H. Xu, Q. Li, D. Xia, Enhanced catalytic ozonation performance of highly stabilized mesoporous ZnO doped $\text{g-C}_3\text{N}_4$ composite for efficient water decontamination, *Appl. Catal. A* 551 (2018) 129–138.
- [44] A. Alhato, R. Kumar, M. Barakat, Integrated ozonation $\text{Ni-NiO}/\text{carbon}/\text{g-C}_3\text{N}_4$ nanocomposite-mediated catalytic decomposition of organic contaminants in wastewater under visible light, *Nanomaterials* 14 (2024) 190.
- [45] R. Chen, F. Fan, C. Li, Unraveling charge-separation mechanisms in photocatalyst particles by spatially resolved surface photovoltage techniques, *Angew. Chem. Int. Ed.* 61 (2022) e202117567.
- [46] S. Gary, Y. Yuan, M. Mortazavi, T. Waite, Caveats in the use of tertiary butyl alcohol as a probe for hydroxyl radical involvement in conventional ozonation and catalytic ozonation processes, *ACS EST Eng.* 2 (2022) 1665–1676.

[47] C. Bernofsky, B. Bandara, O. Hinojosa, Electron spin resonance studies of the reaction of hypochlorite with 5,5-dimethyl-1-pyrroline-N-oxide, *Free Radic. Biol. Med.* 8 (1990) 231–239.

[48] S. Bonke, T. Risse, A. Schnegg, A. Bruckner, In situ electron paramagnetic resonance spectroscopy for catalysis, *Nat. Rev. Methods* 1 (2021) 33.

[49] Y. Zhao, P. Zhang, Z. Yang, L. Li, J. Gao, S. Chen, T. Xie, C. Diao, S. Xi, B. Xiao, C. Hu, W. Choi, Mechanistic analysis of multiple processes controlling solar-driven H_2O_2 synthesis using engineered polymeric carbon nitride, *Nat. Commun.* 12 (2021) 3701.

[50] Y. Jiang, X. Wang, A. Pan, Properties of excitons and photogenerated charge carriers in metal halide perovskites, *Adv. Mater.* 31 (2019) 1806671.

[51] X. Niu, Q. Zhu, S. Jiang, Q. Zhang, J. Photoexcited electron dynamics of nitrogen fixation catalyzed by ruthenium single-atom catalysts, *Phys. Chem. Lett.* 11 (2020) 9579–9596.

[52] L. Lin, H. Ou, Y. Zhang, X. Wang, Tri-s-triazine-based crystalline graphitic carbon nitrides for highly efficient hydrogen evolution photocatalysis, *ACS Catal.* 6 (2016) 3921–3931.

[53] H. Dong, C. Zhang, W. Nie, S. Duan, C. Saggau, M. Tang, M. Zhu, Y. Zhao, L. Ma, O. Schmidt, Interfacial chemistry triggers ultrafast radiative recombination in metal halide perovskites, *Angew. Chem. Int. Ed.* 61 (2022) e202115875.

[54] S. Liu, Y. Hu, H. Xu, Z. Lou, J. Chen, C. Yuan, X. Lv, X. Duan, S. Wang, X. Wu, Directional electron transfer in single-atom cobalt nanozyme for enhanced photo-Fenton-like reaction, *Appl. Catal. B* 335 (2023) 122882.

[55] P. Zhang, T. Tong, Y. Liu, J. Vequizo, H. Sun, C. Yang, A. Yamakata, F. Fan, W. Lin, X. Wang, W. Choi, Heteroatom dopants promote two-electron O_2 reduction for photocatalytic production of H_2O_2 on polymeric carbon nitride, *Angew. Chem. Int. Ed.* 59 (2020) 16209–16217.

[56] B. Xiao, T. Lv, T. Zhou, J. Zhao, X. Kuang, Y. Zhang, D. Wang, J. Zhang, Z. Zhu, Q. Liu, Insights into the interaction effect of CuSA-ZnS for enhancing the photocatalytic hydrogen evolution, *ACS Catal.* 13 (2023) 12904–12916.

[57] J. Wang, Y. Xie, G. Yu, L. Yin, J. Xiao, Y. Wang, W. Lv, Z. Sun, J. Kim, H. Cao, Manipulating selectivity of hydroxyl radical generation by single-atom catalysts in catalytic ozonation: surface or solution, *Environ. Sci. Technol.* 56 (24) (2022) 17753–17762.

[58] J. Wang, G. Yu, Y. Wang, S. Liu, J. Qiu, Y. Xu, Z. Wang, Y. Wang, Y. Xie, H. Cao, Surface density of cobalt single atoms manipulating hydroxyl radical generation via dual pathways: electrons supply and active sites, *Adv. Funct. Mater.* 33 (2023) 2215245.